Fully 3GPP-Compatible Long-Range Sensing for LEO-ISAC: A Window-Grid Processing Framework

Yi Geng[1], Xun Fan[1], Chenfeng Xu[1,2], Yu Zhao[1,2]
[1]Shanghai Institute of Microsystem and Information Technology, Chinese Academy of Sciences, China
[2]State Key Laboratory of Heterogeneous Integrated Microsystem, China
gengyi@mail.sim.ac.cn, fanxun@mail.sim.ac.cn, chenfeng.xu@mail.sim.ac.cn, yu.zhao@mail.sim.ac.cn

arXiv:2609.30653v1 [cs.IT] 25 Sep 2026

***Abstract*—This paper addresses the long-range sensing problem in bistatic low-Earth-orbit integrated sensing and communication (LEO-ISAC) systems. Conventional OFDM-based sensing schemes fail in LEO-ISAC due to excessive propagation delays, which cause cross-symbol misalignment and unequal signal durations. We propose a window-grid processing framework that leverages the deterministic target geometry to resolve both challenges as a pure receiver-side processing: the transmitted sensing signal is 3GPP-compatible. Simulations demonstrate meter-level ranging accuracy for two targets at bistatic ranges beyond 640 km with 100.8 MHz bandwidth.**

***Index Terms*—LEO-ISAC, satellite, OFDM, cyclic prefix, bistatic sensing, range estimation, range-Doppler processing.**

I. Introduction

Integrated sensing and communication (ISAC) has emerged as one of the key technologies of 6G, enabling wireless systems to simultaneously provide data services and sensing [1]. In parallel, low-Earth-orbit (LEO) satellite has attracted interest as a means of providing ubiquitous coverage. The integration of ISAC into LEO satellite systems [2], i.e., *LEO-ISAC*, therefore represents a compelling opportunity: the continuous wide-area illumination afforded by LEO could enable persistent target sensing alongside communication services, with applications spanning aircraft surveillance, space debris detection, and maritime monitoring [3], [4].

An attractive sensing mode for LEO-ISAC is the bistatic mode [5], [6]. As illustrated in Fig. 1, a gateway (GW) acts as the sensing transmitter (TX); low-altitude targets, such as aircraft, reflect the signal; the echoes are received by a satellite (RX) at an altitude of 600 km. Both the GW and satellite employ narrow beamwidths of 0.2° and 2°, respectively [7], to compensate for the significant path loss. The space simultaneously illuminated by both beams is an elongated swath extending along the GW beam direction, approximately 20 km in length and several hundred meters in width.

This bistatic geometry, however, introduces fundamental challenges with no counterpart in terrestrial ISAC systems. The absolute propagation delay exceeds 2 ms (600 km), which would require a cyclic prefix (CP) length of more than 2 ms to avoid inter-symbol interference (ISI) if conventional orthogonal frequency division multiplexing (OFDM)-based sensing schemes were employed [1], an overhead far exceeding the symbol body duration (typically tens of microseconds) and thus unacceptable in practice.

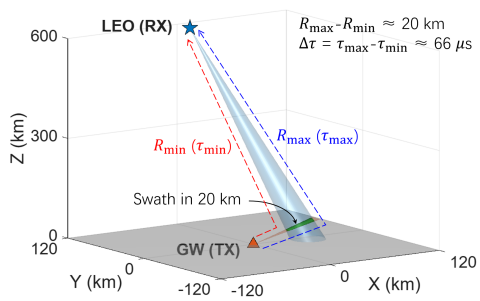

Fig. 1. Illustration of a bistatic LEO-ISAC scenario.

To extend CP-limited sensing range, numerous strategies have been proposed for terrestrial ISAC. One line of work modifies the CP structure itself: Tang et al. [8] proposed an ISI-resistant CP by extracting second-half symbol samples; Jiang et al. [9] developed a CP design with cyclic shifts and inverse phase compensation; Zhou et al. [10] proposed an alternating CP and cyclic postfix structure. A different line of work instead replaces the CP with an alternative signal: Bomfin et al. [11] replaced the CP with a unique word; Ma et al. [12] replaced the CP with a chirp signal. However, all of these works introduce standard modifications of the transmitted signals, which contradicts the lean design principle of 6G standardization [13], and they can only extend the sensing range to at most several kilometers—far from sufficient for LEO-ISAC systems.

In this paper, we identify two challenges for OFDM-based LEO-ISAC, and propose a *window-grid* (*WG*) processing framework that leverages the deterministic swath geometry, enabling long-range bistatic range estimation. In contrast to the aforementioned solutions, the proposed scheme is *fully 3GPP-compatible*: the transmitted sensing signal is unmodified, all novelty resides in receiver-side processing. To the best of our knowledge, this is the first fully standard-compatible scheme that supports ultra-long-range sensing.

II. System Model and Problem Formulation

A. OFDM Signal and Echo Model

Considering the LEO-ISAC scenario in Fig. 1, the TX transmits sensing signals within a time-frequency block comprising M subcarriers and $N_{\rm s}$ symbols, indexed by m and n, respectively. Each symbol body contains $N_{\rm data}$ samples ($T_{\rm data}$

in time), with a CP of $N_{\rm cp}$ samples ($T_{\rm cp}$ in time) prepended, yielding a total symbol length of $N_{\rm sym} = N_{\rm cp}+N_{\rm data}$ samples at a sampling rate $f_{\rm s} = B$, where B is the system bandwidth.

Let the minimum and maximum bistatic ranges for any position within the swath be $R_{\min}$ and $R_{\max}$, respectively. For a target p in the swath, its bistatic delay τ_p satisfies $\tau_{\min} \le \tau_p \le \tau_{\max}$, with $\tau_{\min} = R_{\min}/c$ and $\tau_{\max} = R_{\max}/c$ (c is light speed). The earliest echo from any target in the swath arrives at the LEO satellite at $\tau_{\min}$, and a receive window of length $N_{\rm s}N_{\rm sym} + \Delta\tau f_{\rm s}$ ($\Delta\tau = \tau_{\max} - \tau_{\min}$) samples suffices to capture all target echoes. Consequently, the received baseband signal is indexed relative to the start of this receive window:

$$r[k] = \sum_{p=1}^{P} \alpha_p x[k - \tilde{d}_p] e^{j2\pi f_{D,p}(k+\tau_{\min} f_{\rm s})/f_{\rm s}} + w[k], \quad k = 0, 1, \ldots, N_{\rm s}N_{\rm sym} + \Delta\tau f_{\rm s} - 1, \quad (1)$$

where P is the number of targets in the swath, $x[\,\cdot\,]$ denotes the discrete baseband transmitted sample sequence, $f_{D,p}$ is the bistatic Doppler shift induced by target p and satellite motion, k is the sample index within the receive window (with $k = 0$ corresponding to time $\tau_{\min}$, the rationale of anchoring the window at $\tau_{\min}$ will be detailed in Section III-A), α_p is the echo amplitude, $w[k]$ is additive white Gaussian noise, and

$$\tilde{d}_p = \lfloor (\tau_p - \tau_{\min}) f_{\rm s} \rceil \quad (2)$$

is the sample delay of the p-th target relative to $\tau_{\min}$.

B. Why Terrestrial ISAC Processing Fails for LEO-ISAC

In terrestrial ISAC, the channel estimate can be obtained by element-wise division between the received echo $Y_n[m]$ and the transmitted signal $X_n[m]$ at the same time-frequency resource:

$$H_n[m] = \frac{Y_n[m]}{X_n[m]} = \sum_{p=1}^{P} \alpha_p e^{j2\pi(f_{D,p} n N_{\rm sym}/f_{\rm s} - m\Delta f \tau_p)}. \quad (3)$$

A subsequent 2D-fast Fourier transform (FFT) over $H_n[m]$ yields the range-Doppler (RD) map. The validity of this processing relies on the premise that TX and RX are symbol-aligned, which holds only when the propagation delay $\tau_p \le T_{\rm cp}$. In LEO-ISAC, however, this premise fundamentally collapses: the CP occupies no more than the symbol body ($T_{\rm cp} \le T_{\rm data}$), yet τ_p can exceed 2 ms, far beyond the CP duration. This gives rise to two problems:

Problem 1 — TX-RX symbol misalignment: The received and the transmitted symbols can no longer be symbol-aligned. performing element-wise division between misaligned RX and TX symbols yields pseudo-random data rather than the channel response. The echo energy is thus scattered across the RD map, merely elevating the noise floor instead of forming a discernible peak.

Problem 2 — Unequal durations between TX signal and RX echo in multi-target scenarios: As established in Section II-A, the receive window must span $N_{\rm s}N_{\rm sym} + \Delta\tau f_{\rm s}$ to capture all target echoes—longer than the transmitted signal duration $N_{\rm s}N_{\rm sym}$. This duration mismatch means the received echo and the transmitted signal are of unequal length, making element-wise division in (3) infeasible.

Due to the aforementioned two problems, conventional OFDM-ISAC processing designed for terrestrial scenarios cannot be directly applied to LEO-ISAC. To the best of our knowledge, no OFDM-based sensing scheme has yet been developed that addresses the symbol-misalignment and unequal signal durations inherent to LEO-ISAC.

III. Proposed Window-Grid Processing

In the bistatic LEO-ISAC scenario, a key distinction arises from the beamforming geometry. As shown in Fig. 1, the intersection of the transmit and receive beams forms an elongated swath that constitutes the only space where target echoes can be generated and collected. Consequently, the earliest arrival time $\tau_{\min}$ and the latest arrival time $\tau_{\max}$ can be determined. Leveraging this prior information, we propose a novel WG processing framework tailored for LEO-ISAC. The framework operates entirely at the RX side, no 3GPP modification of the transmitted signal is required.

A. Transmit-Receive Timing

From $t = 0$, the TX transmits a block of sensing signals with $N_{\rm s}$ symbols, followed by a silent guard interval $\Delta\tau$. This interval prevents echoes of the next block from overlapping with the tail of the current receive window, ensuring inter-block isolation at the RX. The RX begins receiving echoes from $t = \tau_{\min}$. The receive window spans $N_{\rm s}N_{\rm sym} + \Delta\tau f_{\rm s}$ samples, covering all echo symbols from all targets. The received sample sequence is exactly $r[k]$ in (1), with $k = 0$ referenced to $\tau_{\min}$. By anchoring the time origin at $\tau_{\min}$, the delay of any target p is expressed as a relative sample offset

$$\tilde{d}_p \in [0, \Delta\tau f_{\rm s} - 1], \quad (4)$$

which folds the millisecond-scale absolute delay into a microsecond-scale interval. This transformation is the key to the proposed framework: instead of designing a CP to cover the entire absolute delay, we only need to handle the much smaller relative delay $\Delta\tau$ determined by the swath.

B. Window-Grid Construction and Processing

To resolve the problems identified in Section II-B, we introduce a *WG construction* composed of multiple WGs. We first describe the pattern of a single WG, and then how multiple WGs are placed on the received sequence $r[k]$.

1) WG pattern: A WG is a combination of $N_{\rm s}$ windows, indexed by $n = 0, 1, \ldots, N_{\rm s} - 1$, whose relative positions replicate the symbol-body timing of the transmitted block, as illustrated in Fig. 2(a). Each window (blue) has a length of $N_{\rm data}$, and consecutive windows are separated by a gap of $N_{\rm cp}$. The *anchor of WG* is defined as the start of the CP preceding its first window (see Fig. 2(a)). If an echo arrived at the anchor of a WG, the n-th window would coincide exactly with the body of the n-th echo symbol.

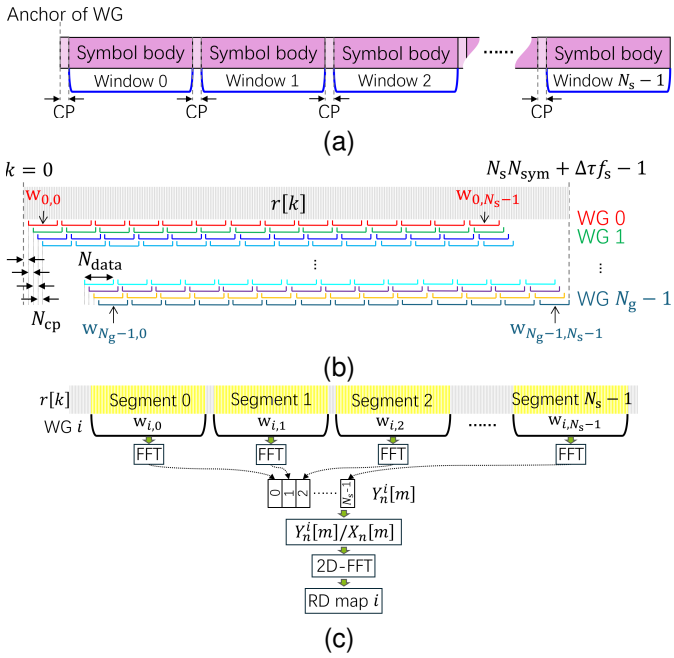

Fig. 2. Illustration of the WG construction: (a) WG pattern; (b) WG capture; (c) WG processing.

2) WG placement: The WG construction is a grid of WGs obtained by shifting the WG pattern in Fig. 2(a) along $r[k]$. As shown in Fig. 2(b), windows with the same color belong to the same WG. WG i places its anchor at $k = iN_{\text{cp}}$, so that its first window starts at $(i+1)N_{\text{cp}}$. The n-th window of WG i, denoted $w_{i,n}$, therefore starts at

$$k_{w_{i,n}} = (i+1)N_{\text{cp}} + nN_{\text{sym}}. \tag{5}$$

By construction, WG i is designed to sense targets whose relative delay $\tilde{d}_p$ lies within one CP from its anchor, i.e.,

$$\tilde{d}_p \in [iN_{\text{cp}},\ (i+1)N_{\text{cp}} - 1]. \tag{6}$$

In other words, WG i is restricted to sensing a range span $[iR_{\text{cp}},\ (i+1)R_{\text{cp}}]$ relative to $R_{\min}$, where $R_{\text{cp}} = \frac{cN_{\text{cp}}}{f_s}$. The relative delay span $\Delta\tau f_s$—far beyond what a single CP could cover—is partitioned into

$$N_g = \left\lceil \frac{\Delta\tau f_s}{N_{\text{cp}}} \right\rceil \tag{7}$$

intervals, which are handled by N_g WGs, respectively. For a target within $[i_d R_{\text{cp}},\ (i_d+1)R_{\text{cp}}]$, WG i_d is called its *designated WG* ($i = i_d$), other WGs are its *undesignated WGs*.

3) WG processing: As illustrated in Fig. 2c, for each WG, the N_s segments extracted by its N_s windows are OFDM-demodulated (FFT) and stacked column-by-column into a matrix $Y_n^i[m]$. An element-wise division by the known transmitted symbols, $Y_n^i[m]/X_n[m]$, followed by a 2D-FFT over the subcarrier (m) and window (n) dimensions produces the RD map of WG i (RD map i).

Through this framework, each window from the designated WG i_d extracts N_{data} samples from the correct echo symbol. To illustrate this mechanism, consider the example in Fig. 3. Only the first window of each WG from WG 0 to WG 30 is shown for clarity. The echo symbols (purple) induced by a target with relative delay $\tilde{d}_p \in [15N_{\text{cp}}, 16N_{\text{cp}}]$ are received by the RX. According to (6), WG 15 is the designated WG (i_d = 15). The first window of WG 15 captures N_{data} samples from echo symbol 0 (green area in Fig. 3). The same holds for every window of WG 15. In contrast, WG 1-14 capture only the front part of echo symbol 0 (yellow area) and WG 16-29 only the rear part (blue area); each extracts a shorter segment than that of WG 15. For WG 0, WG 30 and beyond, the extracted segments (red area) do not overlap with echo symbol 0. This mechanism can be further generalized as: window $w_{i,n}$ of WG i overlaps echo symbol n with length

$$L(\delta_i) = \begin{cases} N_{\text{data}}, & 0 \le \delta_i \le N_{\text{cp}} \quad \text{(Case 1)}, \\ N_{\text{sym}} - \delta_i, & N_{\text{cp}} < \delta_i < N_{\text{sym}} \quad \text{(Case 2)}, \\ N_{\text{data}} + \delta_i, & -N_{\text{data}} < \delta_i < 0 \quad \text{(Case 3)}, \\ 0, & \text{otherwise}, \end{cases} \tag{8}$$

where δ_i is the delay relative to the anchor of WG i (the low boundary in (6)):

$$\delta_i = \tilde{d}_p - iN_{\text{cp}}. \tag{9}$$

Case 1 in (8) is the case for designated WG: $w_{i_d,n}$ extracts N_{data} samples from echo symbol n's body. The following processing in Fig. 2(c) yields a peak (*true peak*) with maximum coherent-accumulation gain $L(\delta_{i_d}) = N_{\text{data}}$ at range

$$R_{i_d} = \frac{c\,\delta_{i_d}}{f_s} \tag{10}$$

relative to the range start of RD map i_d (i.e., $i_d R_{\text{cp}}$). The absolute bistatic range estimation is

$$R_{\text{bi}} = R_{\min} + i_d R_{\text{cp}} + R_{i_d}. \tag{11}$$

Case 2 and 3 are the cases for undesignated WGs: for Case 2, $w_{i,n}$ opens too early and captures only the leading $N_{\text{sym}} - \delta_i$ samples from echo symbol n (the *early side* as illustrated in Fig. 3); for Case 3, it opens too late and captures only the trailing $N_{\text{data}} + \delta_i$ samples (the *late side*). The partial samples captured by undesignated WGs from the correct echo symbols may still produce peaks (*ghost peaks*) at velocity coincides with that of the true peak, and at range

$$R_i = \left(\frac{c\,\delta_i}{f_s}\right) \bmod R_{\text{una}} = \frac{c}{f_s}\left(\delta_i \bmod N_{\text{data}}\right) \tag{12}$$

in RD map i, where $R_{\text{una}} = c/\Delta f$ is the maximum unambiguous bistatic range. The modulo in (12) demonstrates that the periodic nature of ghost peaks, as the inverse FFT (IFFT) over the frequency domain is periodic with R_{una}.

C. Ghost-Peak Analysis and Suppression

As highlighted in [3], the maximum unambiguous range of standard OFDM-ISAC schemes is limited to R_{una}, which is insufficient for the ultra-long-range sensing required in LEO-ISAC. The proposed WG processing addresses this limitation through two mechanisms that resolve ghost peaks and guarantee unambiguous range estimation across the entire swath:

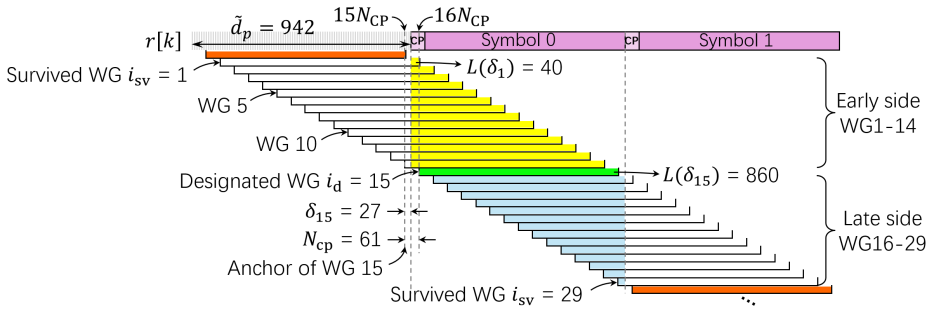

Fig. 3. Samples captured by designated WG 15 and undesignated WGs 0-14 and 16-30.

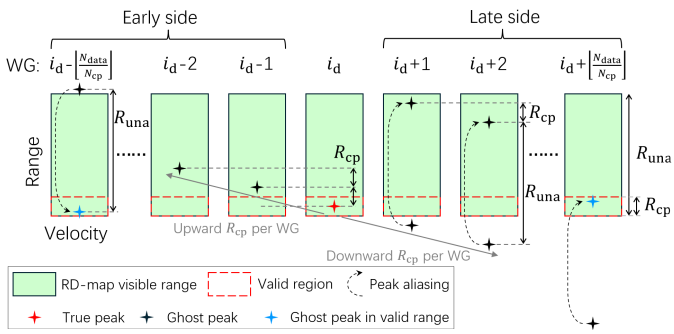

Fig. 4. Schematic of true and ghost peaks in RD maps from different WGs.

a) Cropping resolves most ghost peaks. From (6), WG i is designed to sense the range interval $[iR_{\mathrm{cp}}, (i+1)R_{\mathrm{cp}}]$. However, the RD map of WG i covers a much wider span of $[iR_{\mathrm{cp}}, iR_{\mathrm{cp}} + R_{\mathrm{una}}]$. Since typically $R_{\mathrm{una}} \gg R_{\mathrm{cp}}$, only the leading segment of length R_{cp} within each RD map is valid (the *valid region*); the remaining portion can be discarded. We refer to this operation as *cropping*.

Fig. 4 illustrates several schematic RD maps (green areas) from designated and undesignated WGs, showing the positional relationship between the true peak and ghost peaks. The RD map from the designated WG i_{d} contains the true peak (red star) within the valid region (red dashed box). For WGs on the early side, δ_i increases N_{cp} for each decrement of i relative to $\delta_{i_{\mathrm{d}}}$ (cf. (9)). Consequently, the ghost-peak range R_i (cf. (12)) increases by R_{cp} relative to the true peak for each decrement of i, placing the ghost peaks outside the valid region and thus cropped, causing no ambiguity. In RD map $i_{\mathrm{d}} - \lfloor \frac{N_{\mathrm{data}}}{N_{\mathrm{cp}}} \rfloor$ (the leftmost RD map), the ghost peak falls in the range $[R_{\mathrm{una}}, R_{\mathrm{una}} + R_{\mathrm{cp}}]$, which lies outside the visible range (green area, $[0, R_{\mathrm{una}}]$). This ghost peak is aliased by the IFFT periodicity and reappears in the valid region (blue star), thereby surviving the cropping operation.

On the late side, since δ_i is negative ($-N_{\mathrm{data}} < \delta_i < 0$), the ghost peak decreases by R_{cp} relative to the true peak for each increment of i, and is aliased back into the RD map. However, only the ghost peak from WG $i_{\mathrm{d}} + \lfloor \frac{N_{\mathrm{data}}}{N_{\mathrm{cp}}} \rfloor$ falls within the valid region and survives cropping (the rightmost RD map in Fig. 4). The two WGs $i_{\mathrm{d}} - \lfloor \frac{N_{\mathrm{data}}}{N_{\mathrm{cp}}} \rfloor$ and $i_{\mathrm{d}} + \lfloor \frac{N_{\mathrm{data}}}{N_{\mathrm{cp}}} \rfloor$, which contain the survived ghost peaks, are referred to as *survived WG* ($i = i_{\mathrm{sv}}$).

b) The two ghost-peak survivors are intrinsically weak. The ghost-peak amplitude is determined by $L(\delta_i)$. Combining (8) and (9) yields

$$L(\delta_i) = \begin{cases} N_{\mathrm{sym}} - \tilde{d}_p + iN_{\mathrm{cp}}, & \text{(Case 2: early side)}, \\ N_{\mathrm{data}} + \tilde{d}_p - iN_{\mathrm{cp}}, & \text{(Case 3: late side)}. \end{cases} \tag{13}$$

From (8) and (13), moving one WG away from i_{d} in either direction reduces $L(\delta_i)$ by N_{cp} relative to $L(\delta_{i_{\mathrm{d}}}) = N_{\mathrm{data}}$, as clearly illustrated in Fig. 3. Consequently, the ghost-peak amplitude decays monotonically and symmetrically as i moves away from i_{d}. The two survived WGs $i_{\mathrm{sv}} = i_{\mathrm{d}} - \lfloor \frac{N_{\mathrm{data}}}{N_{\mathrm{cp}}} \rfloor$ and $i_{\mathrm{sv}} = i_{\mathrm{d}} + \lfloor \frac{N_{\mathrm{data}}}{N_{\mathrm{cp}}} \rfloor$, capture

$$L(\delta_{i_{\mathrm{sv}}}) = N_{\mathrm{data}} - (\lfloor \frac{N_{\mathrm{data}}}{N_{\mathrm{cp}}} \rfloor - 1)N_{\mathrm{cp}} - \delta_{i_{\mathrm{d}}} \tag{14}$$

samples from the correct echo symbols. Given that $0 \le \delta_{i_{\mathrm{d}}} < N_{\mathrm{cp}}$, it follows that $L(\delta_{i_{\mathrm{sv}}}) \le N_{\mathrm{cp}}$. The survived ghost peaks are therefore attenuated by at least $20\log_{10}(N_{\mathrm{data}}/N_{\mathrm{cp}})$ dB relative to the true peak (approximately 23 dB for a 3GPP-standard symbol configuration with 6.5% CP overhead). In the high-path-loss LEO-ISAC scenario, this attenuation is typically sufficient to push the survived ghost peaks below the noise floor.

D. Discussions

Since each WG requires N_{s} OFDM demodulations (FFTs) followed by one 2D-FFT, the overall computational complexity of WG processing framework is

$$C_{\mathrm{WG}} = N_{\mathrm{g}} N_{\mathrm{s}} M(\log_2 M + \log_2 N_{\mathrm{s}}). \tag{15}$$

Although C_{WG} scales linearly with N_{g}, the N_{g} WG branches are mutually independent—each operates on its own set of windows and produces its own RD map—so the framework is parallel and can be distributed across parallel processing units (e.g., multi-core CPUs) to meet real-time requirements.

3GPP is currently exploring extended CP lengths as a means of increasing the CP-limited sensing range for terrestrial ISAC. Any such standardized CP increase would proportionally reduce N_{g}, and hence lower the computational complexity of the proposed framework.

The WG framework can also assist satellite communication. The absolute delay is a nuisance parameter in communication,

TABLE I
PARAMETERS USED IN THE SIMULATION

Parameter	Symbol	Value
Light speed	c	299792458 m/s
Waveform		CP-OFDM
Modulation		QPSK
Carrier frequency	f_{c}	24 GHz
Overall bandwidth	B	103.2 MHz
Guard band	B_{guard}	2.4 MHz
Effective bandwidth for sensing	B_{eff}	100.8 MHz
Subcarrier spacing	Δf	120 kHz
Subcarriers in one block	M	840 subcarriers
Symbols in one block	N_{s}	700 symbols
Sample rate	$f_{\mathrm{s}} = B$	103.2 MHz
Duration of a sample	$T_{\mathrm{sample}} = \frac{1}{B}$	9.6899 ns
CP duration in samples	N_{cp}	61 samples
Range span per CP duration	R_{cp}	177.2 m
Symbol body duration in samples	$N_{\mathrm{data}} = \frac{B}{\Delta f}$	860 samples
Symbol duration in samples	N_{sym}	921 samples
Maximum unambiguous range	$R_{\mathrm{una}} = \frac{c}{\Delta f}$	2498.3 m
Number of WGs	N_{g}	112
TX (GW) peak power	P_{TX}	1000 W
TX antenna and beamforming gain	G_{TX}	55 dB
RX antenna and beamforming gain	G_{RX}	38 dB
Noise figure	NF	2.9 dB
Reference temperature	T_{ref}	290 K

where it is masked by synchronization, but is the parameter of interest in sensing. When synchronization is unavailable, e.g., during initial access, the WG processing can be reused as a structured timing-acquisition search. Since WG processing operates on the unmodified 3GPP waveform and its FFT outputs can be shared by both communications and sensing, it provides a common receiver structure for both communications and sensing.

IV. SIMULATIONS

A. Simulation Setup

We consider the bistatic LEO-ISAC scenario depicted in Fig. 1. At time $t = 0$, the TX is located at (0, 0, 0), while the satellite is at (0, 100, 600) km with a velocity of (7500, 0, 0) m/s, simulating a LEO motion. Both the TX and the satellite steer their beam boresights toward (51, 0, 7.5) km, forming a swath intersection. Within this swath, the minimum and maximum bistatic ranges are R_{min} = 644.236 km and R_{max} = 663.961 km, respectively, yielding a relative delay $\Delta\tau$ of 65.8 μs. The parameters used in the simulation are listed in Table I. A guard band is excluded from the bandwidth B, leaving an effective bandwidth B_{eff} for sensing. In particular, a 3GPP-compatible symbol structure for Δf = 120 kHz is adopted, i.e., T_{cp} = 0.59 μs (N_{cp} = 61) and symbol body of T_{data} = 8.33 μs (N_{data} = 860), so that each WG covers a bistatic range span of R_{cp} = 177.2 m. Based on (7), the WG number required to cover $\Delta\tau$ is 112.

Two aircraft targets ($p1$ and $p2$) are placed within the swath at (43, 0, 6.4) km and (60, 0, 9) km, respectively, both with velocity (200, 0, 0) m/s and RCS of 100 m^2. The echo amplitude α_p is computed from the bistatic radar equation using the power, antenna gain, and noise parameters listed in Table I. Their true bistatic ranges, computed from the GW and LEO positions, are 646.9718 km and 663.0673 km, respectively. From (2), (6), and (9), target $p1$ ($\tilde{d}_{p1}$ = 942 samples) falls into the delay range of WG 15 (δ_{15} = 27 samples) and is therefore expected to appear in RD map 15, while target $p2$ ($\tilde{d}_{p2}$ = 6482 samples) falls into WG 106 (δ_{106} = 16 samples). Since $p2$ lies near the far edge of the swath, its echo extends close to the end of the receive window, so the two targets' echoes jointly span a duration approaching $N_{\mathrm{s}}T_{\mathrm{sym}} + \Delta\tau$, exceeding the transmitted signal duration $N_{\mathrm{s}}T_{\mathrm{sym}}$—exactly the unequal-duration situation identified as Problem 2 in Section II-B.

B. Simulation Results

Fig. 5 shows the representative RD maps out of the 112 maps generated by the framework. In Fig. 5(a) (RD map 15), a distinct peak is observed at $\hat{R}_{15,p1}$ = 72.5 m and a velocity of -161 m/s. Using (11), the estimated bistatic range is 646.9665 km ($R_{\mathrm{min}} + 15R_{\mathrm{cp}} + \hat{R}_{15,p1}$). The true range is 646.9718 km, yielding a range error of 5.3 m. In Fig. 5(b) (RD map 106), a peak is observed at $\hat{R}_{106,p2}$ = 41.6 m and a velocity of -264 m/s; the estimated range is 663.0608 km ($R_{\mathrm{min}} + 106R_{\mathrm{cp}} + \hat{R}_{106,p2}$) against the true 663.0673 km, a range error of 6.5 m. Both targets are observed within the valid region in their designated RD maps: the millisecond-scale absolute delays spanning hundreds of symbols are correctly absorbed by the WG alignment (Problem 1 resolved), and the overlapping echoes exceeding the transmitted signal duration are handled without element-wise division mismatch (Problem 2 resolved). The successful detection of two targets validates the framework's capability for multi-target sensing.

The velocity estimate, however, deviates significantly from the true velocity. This discrepancy arises because the satellite's orbital motion has not been compensated in WG processing. Doppler compensation based on known ephemeris will be incorporated in future work to recover the target's velocity.

We next verify the ghost-peak analysis in Section III-C. For $p1$ ($\tilde{d}_{p1}$ = 942), ghost peaks are predicted to occur in RD map 1-14 (early side) and 16-29 (late side) because partial samples are captured from correct echo symbols, as illustrated in Fig. 3. Figs. 5(c)-5(e) shows three of them: RD maps 10, 5, and 1. Whether ghost peaks cause ambiguity depends on their locations relative to the valid region $[0, R_{\mathrm{cp}}]$. As illustrated in Fig. 5(c), WG 10 (five steps away from the designated WG 15) produces a ghost peak at 959.7 m (72.5 + $5R_{\mathrm{cp}}$), and in Fig. 5(d), WG 5 (ten steps away) at 1841.9 m (72.5 + $10R_{\mathrm{cp}}$). These ghost peaks shift progressively upward as i moves away from i_{d} on the early side, consistent with the positional relationship depicted in Fig. 4. Both fall outside the valid region [0, 177.2] m and are therefore discarded by cropping.

However, as i continues to decrease, the ghost peak shifts further until δ_i approaches N_{data}, at which point it moves out of the RD map and wraps back into the opposite end via the modulo operation in (12). For the survived WG $i_{\mathrm{d}} - \lfloor \frac{N_{\mathrm{data}}}{N_{\mathrm{cp}}} \rfloor$ = 1, the extrapolated ghost-peak location 2553.3 m (72.5 + $14R_{\mathrm{cp}}$) exceeds R_{una} = 2498.3 m and would be wrapped back to 61 m inside the valid region, exactly as depicted in

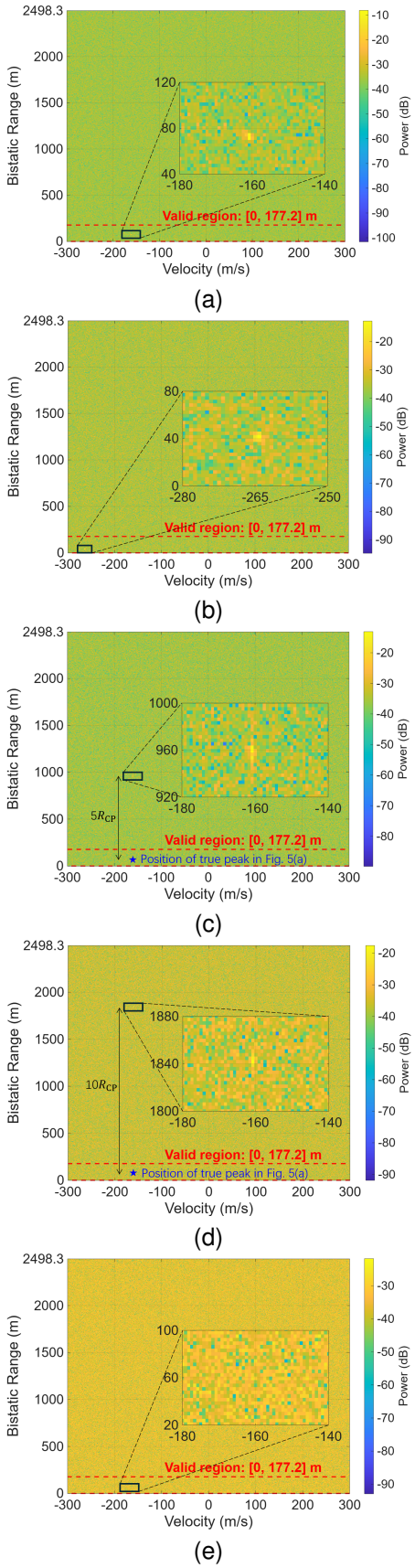

Fig. 5. RD maps: (a) RD map 15 (WG 15); (b) RD map 106 (WG 106); (c) RD map 10 (WG 10); (d) RD map 5 (WG 5); (e) RD map 1 (WG1).

the leftmost RD map of Fig. 4. However, no peak is visible in RD map 1 (Fig. 5(e)). This is because the survived WG 1 captures only $L(\delta_1) = 40$ samples (cf. (14)) from the correct echo symbols, yielding an attenuation of $20\log_{10}(860/40) = 26.6$ dB relative to the true peak. In the high-path-loss LEO-ISAC scenario, this substantial attenuation is sufficient to push the survived ghost peak below the noise floor.

V. Conclusions

This paper identified two fundamental challenges in LEO-ISAC that render terrestrial OFDM sensing inapplicable, and proposed a window-grid processing framework that resolves both while keeping the transmitted signal fully 3GPP-standard-compatible, all novelty resides at the receiver. Simulations at bistatic ranges beyond 640 km demonstrated meter-level range accuracy for two targets. Future work includes ephemeris-based Doppler compensation and range-migration correction.

References

[1] Q. Dai, Y. Zeng, H. Wang, C. You, C. Zhou, H. Cheng, X. Xu, S. Jin, A. Lee Swindlehurst, Y. C. Eldar, R. Schober, R. Zhang, and X. You, "A tutorial on MIMO-OFDM ISAC: From far-field to near-field," *IEEE Communications Surveys & Tutorials*, vol. 28, pp. 4319–4358, 2026.

[2] L. You, Y. Zhu, X. Qiang, C. G. Tsinos, W. Wang, X. Gao, and B. Ottersten, "Ubiquitous integrated sensing and communications for massive MIMO LEO satellite systems," *IEEE Internet of Things Magazine*, vol. 7, no. 4, pp. 30–35, 2024.

[3] Z. Wei, H. Liu, Y. Geng, Z. Feng, G. Gui, and K. Zheng, "ISAC-empowered LEO constellation networked sensing: Challenges and opportunities," *IEEE Wireless Communications*, vol. 33, no. 3, pp. 47–56, 2026.

[4] Y. Zhang, F. Soualle, M. F. Keskin, Y. Liu, L. Wu, J. A. d. Peral-Rosado, B. Shankar M. R., G. Seco-Granados, H. Wymeersch, and T. Y. Al-Naffouri, "Distributed integrated sensing, localization, and communications over LEO satellite constellations," *IEEE Wireless Communications*, vol. 33, no. 3, pp. 57–65, 2026.

[5] J. Park, J. Seong, Y. Mao, W. Shin, and B. Ottersten, "A bistatic ISAC framework for LEO satellite systems: A rate-splitting approach," *IEEE Transactions on Aerospace and Electronic Systems*, vol. 61, no. 6, pp. 17 282–17 301, 2025.

[6] Y. Zhang, Y. Gang, T. Mao, R. Liu, M. Hua, and Q. Wu, "LEO satellite-enabled ISAC: Bistatic framework and beamforming design," *IEEE Transactions on Vehicular Technology*, pp. 1–15, 2026.

[7] M. Höyhtyä, *Satellite Communications and Networks*, ser. Textbooks in Telecommunication Engineering. Cham, Switzerland: Springer, 2025.

[8] A. Tang, Q. Zhao, X. Wang, and W. Qu, "ISI-resistant reference signal design and processing for OFDM integrated communications and long-range radar sensing," *IEEE Communications Letters*, vol. 28, no. 6, pp. 1322–1326, 2024.

[9] Q. Jiang, X. Sun, D. Wang, C. Pan, and J. Wang, "Scalable long-distance ISAC signal design for OFDM systems with theoretical analysis and practical validation," *IEEE Wireless Communications Letters*, vol. 14, no. 7, pp. 1894–1898, 2025.

[10] Y. Zhou, C. Xu, J. Liu, W. Wang, and F. Gao, "Improving ISAC system long-range sensing with alternating cyclic prefix and postfix signals," in *2024 IEEE 35th International Symposium on Personal, Indoor and Mobile Radio Communications (PIMRC)*, 2024, pp. 1–6.

[11] R. Bomfin and M. Chafii, "Unique word-based frame design for bistatic ISAC with time-domain filtering," in *GLOBECOM 2024 - 2024 IEEE Global Communications Conference*, 2024, pp. 4720–4725.

[12] Y. Ma, S. Xia, Z. Wang, D. Chen, and Z. Yuan, "Can we achieve any-length cyclic prefix for flexible ISAC coverage?" in *ICC 2025 - IEEE International Conference on Communications*, 2025, pp. 5964–5969.

[13] W. Chen, L. Liu, X. Liu, E. G. Larsson, M. El Jaafari, and T. Q. S. Quek, "Toward standardization of 6G and nextG: Key technologies to enable fundamental enhancements," *IEEE Journal on Selected Areas in Communications*, vol. 44, pp. 4333–4365, 2026.